Chemical Engineering Science 296 (2024) 120207

Contents lists available at ScienceDirect

Chemical Engineering Science

journal homepage: www.elsevier.com/locate/ces

New insights on antimony removal and recovery from water and wastewater using iron-coated cork granulates: Desorption on batch and fixed-bed column systems

Mariko A. Carneiro [a,b,*], Tânia A. Silva [a,b], Pedro J.S. Teixeira [a,b], Rui A.R. Boaventura [a,b], Cidália M.S. Botelho [a,b], Ariana M.A. Pintor [a,b,*]

[a] Laboratory of Separation and Reaction Engineering – Laboratory of Catalysis and Materials (LSRE-LCM), Department of Chemical Engineering, Faculty of Engineering, University of Porto, Rua Dr. Roberto Frias 4200-465 Porto, Portugal

[b] ALiCE - Associate Laboratory in Chemical Engineering, Faculty of Engineering, University of Porto, Rua Dr. Roberto Frias 4200-465 Porto, Portugal

ARTICLE INFO

Keywords:
Adsorption
Desorption
Kinetics
Isotherms
Breakthrough curve

ABSTRACT

This work investigated Sb adsorption–desorption using iron-coated cork granulates (ICG) in both batch and continuous modes to evaluate the materiaĺs adsorption and regeneration performance, as well as the possibility of antimony recovery. A fixed-bed column filled with ICG, demonstrated maximum adsorption capacities of 13 ± 2 mg g^{-1} and 10 ± 1 mg g^{-1} for Sb(III) and Sb(V), respectively, at pH 3. ICG was able to remove Sb within the WHO guideline of 20 µg/L at pH 6. Among the different classes of eluents tested for Sb(V) desorption, the acids achieved the highest desorption rates – 81 ± 9 % and 66 ± 8 % for HCl 1 M and ascorbic acid 0.1 M, respectively. The desorption kinetics showed that HCl 1 M reached equilibrium in 4 h, but ascorbic acid 0.1 M took 16 h. This work presents an ecological emerging solution for antimony removal and recovery from water and wastewater.

List of acronyms.

AD	Adsorption
DE	Desorption
EDS	Electron dispersive X-ray spectroscopy
FAAS	Flame atomic absorption spectrometry
FR	Flow rate
GFAAS	Graphite furnace atomic absorption spectrometry
ICG	Iron-coated cork granulates
MTZ	Mass transfer zone
PET	Polyethylene terephthalate
SE	Standard error
SEM	Scanning electron microscopy
SDG	Sustainable Development Goals
S/L	solid/liquid ratio
WHO	World Health Organization
List of symbols	
a	initial rate of adsorption/desorption (mg g^{-1} h^{-1})
a_{Ya}	Yan model empirical parameter

(*continued on next column*)

(*continued*)

b	coverage scale factor that corresponds to the reciprocal of the coverage at which the adsorption/desorption rate has fallen to 1/e of its initial value (g mg^{-1})
BV_b	bed volume at breakthrough (L)
BV_s	bed volume at saturation (L)
C	concentration of adsorbate (mg/L)
C_f	final concentration of the adsorbate (mg L^{-1})
C_i	initial concentration of the adsorbate (mg L^{-1})
k_1	pseudo-first-order kinetic constant (h^{-1})
k_2	pseudo-second-order kinetic constant (g mg^{-1} h^{-1})
K_F	Freundlich constant ($mg^{(1-1/n)}$ $L^{1/n}$ g^{-1})
K_L	Langmuir constant (L mg^{-1})
m	mass of adsorbent (g)
MTZ	mass transfer zone length (cm)
n	dimensionless parameter related to adsorbent-adsorbate affinity
q_{ad}	adsorption capacity (mg g^{-1})
q_b	adsorption capacity at breakthrough (mg g^{-1})
q_d	desorption capacity (mg g^{-1})
q_e	adsorbed/desorbed amount at equilibrium (mg g^{-1})

(*continued on next page*)

* Corresponding authors at: Laboratory of Separation and Reaction Engineering – Laboratory of Catalysis and Materials (LSRE-LCM), Department of Chemical Engineering, Faculty of Engineering, University of Porto, Rua Dr. Roberto Frias 4200-465 Porto, Portugal. ALiCE - Associate Laboratory in Chemical Engineering, Faculty of Engineering, University of Porto, Rua Dr. Roberto Frias 4200-465 Porto, Portugal.

E-mail addresses: mariko.carneiro@fe.up.pt (M.A. Carneiro), ampintor@fe.up.pt (A.M.A. Pintor).

https://doi.org/10.1016/j.ces.2024.120207
Received 31 January 2024; Received in revised form 21 April 2024; Accepted 30 April 2024
Available online 11 May 2024

(*continued*)

q_{max}	maximum adsorption capacity (mg g^{-1})
q_s	adsorption capacity at the saturation point (mg g^{-1})
q_t	adsorbed/desorbed amount at time t (mg g^{-1})
q_{Ya}	Yan model predicted adsorption capacity (mg g^{-1})
Q	flow rate (mL min^{-1})
r^2	coefficient of determination
t	time (h)
t_b	breakthrough time (h)
t_s	saturation time (h)
T	temperature (°C)
V	solution volume (L)
V_b	breakthrough volume (L)
V_s	saturation volume (L)
yb	arsenic removal efficiency at breakthrough (%)
ys	arsenic removal efficiency at saturation (%)

1. Introduction

Antimony is a hazardous pollutant and toxic for humans which can enter the body through oral, skin, and inhalation forms (Nishad and Bhaskarapillai, 2021). In surface and groundwaters, antimony (Sb) usually exists in two oxidative states, as the inorganic oxyanions, Sb(III) and Sb(V) (Zhang et al., 2022b). The less oxidized form is ten times more harmful than the more oxidized form (Qi et al., 2021).

There are various sources of contamination of water bodies by antimony, from natural erosion of antimony ores or minerals to anthropogenic sources, such as industrial and mining activities. A recent concern is related to the leaching of antimony from PET plastics (Nishad and Bhaskarapillai, 2021). The industrial application of antimony is wide, for example, in the production of semiconductors, infrared detectors, acid batteries, ceramics, glasses, plastics, and flame retardants (Dembele et al., 2022; Zhang et al., 2021b).

Sb levels in drinking water may not exceed 20 μg/L per liter, as guidelines from the World Health Organization suggest (WHO, 2022). More restricted limits were established by the European Union (EU) of 10 μg L^{-1} (European Union, 2020), the United States (USA) and Canada of 6 μg L^{-1} (Canada, 1999; EPA, 2002), and China of 5 μg L^{-1} ((MOH), 2006). Currently, the presence of antimony in the aquatic systems of countries like China, the USA, Mexico, Australia, Spain, Slovakia and New Zealand is a serious problem (Herath et al., 2017). High levels of antimony were also reported in other countries in the water close to abandoned mining areas: 15,000 μg L^{-1} in Italy (Cidu et al., 2013), 2,500 μg L^{-1} in Poland (Lewińska et al., 2018), 2,138 μg L^{-1} in Portugal (Carvalho et al., 2014), 750 μg L^{-1} in Ghana (Serfor-Armah et al., 2006), and 271.6 μg L^{-1} in Turkey (Kurt et al., 2021). In wastewaters, the concentrations of Sb are much higher than in drinking water, and the legal limit varies by industry and country (Gan et al., 2023),

Antimony's removal from water and wastewater can be achieved by different techniques or even a combination of them, based on the elemenťs concentration in solution and on the quality requirements for the treated water, such as coagulation-flocculation-sedimentation, membrane separation technologies, electrocoagulation, phytoremediation, adsorption (AD), and ion exchange (Nishad and Bhaskarapillai, 2021; Ungureanu et al., 2015). Among these, ion exchange and adsorption are considered more suitable for industrial applications (Nishad et al., 2017; Zhang et al., 2021a). Adsorption is a well-known technology used to remove contaminants from water. Recent innovations have improved it towards reducing costs and increasing efficiency (Bortone et al., 2021; Chen et al., 2022; R et al., 2022).

Various adsorbents were demonstrated to be capable of removing antimony from water under legal limits; however, their production costs on a large scale can be a hindrance to their commercial application (Cheng et al., 2022). Hence, it is important to develop adsorbents using abundant and low-cost materials, even if their performance may be slightly lower (Bacelo et al., 2022; Ungureanu et al., 2015). Still, only a few studies have reported antimony uptake by naturally derived materials, such as pine bark tannin resin (Bacelo et al., 2022; Bacelo et al., 2018), marine algae (Ungureanu et al., 2015; Ungureanu et al., 2017), Mn-coated biochar (Jia et al., 2020), plant waste (Iqbal et al., 2013), metal-loaded orange waste (Biswas et al., 2009), and iron-treated fungi aerobic granules (Wan et al., 2014). However, certain inexpensive adsorbents indicated are not sufficiently stable to be used in "clean" applications, while others have inadequate particle size or mechanical characteristics, which can lead to clogging issues in packed beds (Bacelo et al., 2018).

Iron-coated cork granulates (ICG) were investigated for pnictogen adsorption, and good uptake capacities for antimony, arsenic, and phosphorus were found (Carneiro et al., 2022b; Pintor et al., 2021; Pintor et al., 2020a; Pintor et al., 2020b; Pintor et al., 2018). Antimony adsorption onto ICG has so far only been studied in batch mode. However, data from continuous operation are more reliable for scaling up adsorption processes applied to industrial effluents (Thirunavukkarasu et al., 2021). Previous research on the regenerability of arsenic-loaded iron-coated cork granulates (Carneiro et al., 2022a) revealed that the adsorbent was stable and suitable for adsorption in fixed-bed columns.

Given the commercial value of antimony and its projected scarcity (Cole-Hamilton, 2020), it is worthwhile to investigate its recovery after removal from water (Bacelo et al., 2022). Furthermore, the regeneration of biosorbents via desorption is one of the most often proposed strategies for valorizing exhausted biosorbents saturated with metals and metalloids (Bădescu et al., 2018). Hence, it is important to undertake a study on regeneration to gain a deeper insight into how biosorbents recycle and to contribute towards minimizing the need for raw materials, energy, time, and reagents spent in the process (Adegoke et al., 2022). Studies on the valorization of wastewater are an important strategy for a more responsible and sustainable future.

This work investigated antimony adsorption in aqueous solution by ICG, an activated biosorbent, and the subsequent desorption in batch and continuous modes aiming at both drinking water treatment and wastewater treatment, and resource recovery. The outcome of this research contributes to the "2030 Agenda for Sustainable Development", mainly regarding the Sustainable Development Goal (SDG) 6 of "Clean Water and Sanitation" and 12 of "Responsible Consumption and Production" (UN, 2016).

2. Materials and methods

2.1. Materials

Stock solutions of Sb(III) were produced by diluting antimony trichloride ($SbCl_3$) (ACS reagent, Acrós Organics) in 0.1 % (v/v) HCl. Stock solutions of Sb(V) were produced by diluting potassium hexahydroxoantimonate ($KSb(OH)_6$) (Aldrich) in distilled water. A distilled water dilution of the stock solutions was performed to achieve the desired working concentration.

Iron-coated cork granulates (ICG) were manufactured according to the methodology optimized by the research group, as described by Pintor et. al. (2018). In brief, cork granulates were put in contact with a $FeCl_3$ 0.05 M solution of pH 7.0, at 20 g/L, in a rotating shaker at 20 rpm, for 24 h, at room temperature. Following the coating time, the granulates were washed with distilled water until the iron excess was removed and put to dry for 24 h.

The desorption eluents were prepared by diluting the following chemicals in distilled water: sodium hydroxide (NaOH) pearls 99.14 % (Labsolve), sodium carbonate anhydrous Na_2CO_3 99.5 % (Merck), disodium ethylenediaminetetraacetate (EDTA) > 98.5 % (May & Baker), nitric acid (HNO_3) 68 % (VWR), HCl 37 % (VWR), citric acid (99.5–102.0)% (Panreac), ascorbic acid (99.0–100.5 %) (VWR), tartaric acid ≥ 99.5 % (Merck), and NaCl ≥ 99.5 % (Merck). All reagents were of analytical grade.

2.2. Analytical methods

2.2.1. Antimony

The concentration of Sb(III) / Sb(V) was determined by measuring total antimony by flame atomic absorption spectrometry (FAAS) (GBC 932 Plus) between 2–50 mg L^{-1} and graphite furnace atomic absorption spectrometry (GFAAS) (GBC GF 3000, SenAA Dual) between 20–100 µg L^{-1}. The operating conditions for both spectrometers were 8 mA lamp current, 217.6 nm wavelength and 0.2 nm slit width. In GFAAS, a Ni solution of 50 mg L^{-1} (prepared from a commercial standard) was used as a chemical matrix modifier.

2.2.2. Iron

Iron concentrations were determined by measuring total iron concentration by FAAS (GBC 932 Plus) in the range of 0.25–5 mg L^{-1} under an air-acetylene flame, a slit width of 0.2 nm, at 8 mA lamp current and a wavelength of 248.3 nm.

2.3. Adsorption in continuous mode

The lab-scale system employed for the adsorption of Sb(V) and Sb (III) onto iron-coated cork granules in continuous mode consisted of various components. These included a glass column (*Chromaflex®*) (diameter = 2.5 cm and length = 15 cm), an influent reservoir with a capacity of 50 L, an effluent reservoir with a capacity of 30 L, a peristaltic pump *(Hei-FLOW Advantage 01, Heidolph*), a thermostatic bath (*DIGIT-COOL, J.P. SELECTA*), and an automatic sample collector (*GILSON, FC-203B*). A representation of the lab-scale adsorption system is shown in Fig. S1.

The fixed-bed column was operated in a downward flow due to the adsorbent's low density. ICG were hydrated in distilled water and vacuumed before each experiment to minimize the air trapped in the pores. Next, the adsorbent was added to the column, which was then operated for two hours with distilled water under the same operational conditions previously optimized for arsenic removal (Carneiro et al., 2022b): 5 mL min^{-1} of flow rate (FR), 12 cm of bed height (6 g of ICG), and 20.0 ± 0.3 °C of temperature. The experimental breakthrough parameters were calculated using the equations mentioned in a previous article with a similar setup (Carneiro et al., 2022b).

The Yan model (Yan et al., 2001) (Eq. S.5) was fitted to the experimental results and the theoretical parameters were obtained.

2.4. Adsorption on a batch operation mode

Batch adsorption of antimony was carried out using a mixing rotator (SB3, Stuart) operating at 20 rpm within a thermostatic cabinet operating at 20.0 ± 0.5 °C, with a solid-to-liquid (S/L) ratio of 2.5 g L^{-1}. After contact, the adsorbent was separated by filtering it through cellulose acetate membrane filters (0.45 µm pore size), and the concentration of antimony was measured in the solution. More details on batch methodological procedures were described in previous works (Pintor et al., 2021; Pintor et al., 2020a). The total iron concentration was additionally determined to observe the release of iron from the adsorbent.

Equilibrium experiments were performed for Sb(III) at pH 3, with a fixed initial concentration of 10 mg L^{-1}. The S/L was varied at values of 0.5, 1.0, 2.0, 3.0, 4.0 and 5.0 g/L. The contact time for the experiments was fixed as 24 h.

The adsorption kinetics was evaluated for Sb(III) at pH 3.0, with initial concentrations of 1 and 15 mg L^{-1}, for contact times of 0.25, 0.5, 1, 2, 4, 8, 16 and 24 h; and 0.25, 0.5, 1, 2, 4, 8, 16, 24 and 48 h, respectively.

The adsorbed amount after each experiment, q_{ad}, was obtained using an equation of mass balance (Eq. (S.1)).

2.4.1. Kinetic models

Both adsorption and desorption kinetic data were assessed using the pseudo-first-order model (Eq. S.2), pseudo-second-order model (Eq. S.3), and Elovich model (Eq. S.4) (Elovich and Larionov, 1962), whose equations are shown in Supplementary Materials.

Non-linear regression analysis was performed using *CurveExpert Professional* v. 2.6.4 to fit the kinetic models to the experimental results.

2.5. Desorption in batch mode

Desorption tests were conducted using different eluents at different concentrations to remove Sb(V) from the saturated ICG. Only the Sb(V) species was tested because it is the most prevalent oxidation state of the element in water. The eluents used as follows: base – NaOH (0.1 M and 0.5 M); acid – HCl (from 0.1 M to 1 M), tartaric acid (0.5 M), citric acid (from 0.1 M to 1 M), ascorbic acid (from 0.001 M to 1 M); salt and complexing agents – NaCl (0.5 M), Na_2CO_3 (0.5 M), and EDTA (0.5 M); and distilled water. The assays were carried out using antimony saturated-ICG containing 10 ± 1 mg Sb(V)/g ICG. The contact time in desorption tests was 24 h. Fig. S2 illustrates a schematic diagram of the adsorption and desorption assays carried out in batch mode.

Ascorbic acid 0.1 M and HCl 1 M were used as eluents to study the desorption kinetics of Sb(V). For that, 0.25, 0.5, 1, 2, 4, 8, 16 and 24 h were the contact times. The assays were carried out using antimony saturated-ICG containing 10 ± 1 mg Sb(V)/g ICG, at a fixed temperature of 20.0 ± 0.5 °C and a S/L ratio of 2.5 g/L.

A mixing rotator was used to agitate the solutions at a speed of 20 rpm. Following the previously specified contact times, filtration was carried out with a 0.45 µm acetate cellulose filter. Subsequently, the filtrated solution was analyzed for the total concentration of Sb by FAAS. The desorbed amount of Sb (q_d, mg g^{-1}) was calculated according to Eq. (S.6).

To determine the amount of iron that leached from the adsorbent, the total amount of dissolved iron in the aforementioned solutions was determined using FAAS.

All the batch assays were carried out in duplicate, and the results presented as the average.

2.6. Desorption in continuous mode

Cycles of adsorption and desorption were performed to evaluate how effectively regenerated ICG can remove Sb(V) from an aqueous solution. For adsorption, the column was fed by a solution of 5 mg L^{-1} of Sb(V) at the operating conditions described in section 2.4. After bed saturation, the column was fed by ascorbic acid 0.1 M in the same operating conditions of adsorption. After desorption was complete, distilled water was pumped by the column at the same flow rate to remove the acid.

2.7. Adsorption in continuous mode using recycled iron-coated cork granulates

After two adsorption–desorption cycles in continuous mode using ascorbic acid 0.1 M as eluent, as described in section 2.6, the ICG was recycled by undergoing a new iron coating. The desorbed ICG were put in contact with a $FeCl_3$ 0.05 M solution of pH 7.0, for 24 h, then washed with distilled water until the iron excess was removed, as described in section 2.1. Then, another adsorption cycle was carried out under the conditions described in section 2.3 to assess the performance of the recycled adsorbent.

2.8. Material characterization

Few studies explore the material changes before and after desorption. In this work, the material was characterized by iron content and SEM—EDS to evaluate the effect of desorption on its chemical and structural properties.

2.8.1. Acid digestion

The iron content of the ICG was assessed before and after regeneration. Each adsorbent material was digested in glass tubes connected to condensers with a mixture of 5.0 mL distilled water, 4.0 mL HNO_3 65 % (analytical grade, VWR), and 12.0 mL HCl 37 % (analytical grade, VWR). The total dissolved iron was determined by FAAS after the digested solution had been filtered and diluted with distilled water. The iron content was calculated by mass balance.

2.8.2. SEM-EDS

Scanning electron microscopy coupled with energy-dispersive X-ray spectroscopy (SEM-EDS) was used to determine the surface morphology and elemental components of the adsorbent. The SEM / EDS analysis was conducted using a High resolution (Schottky) Environmental Scanning Electron Microscope with X-Ray Microanalysis and Electron Backscattered Diffraction analysis: FEI Quanta 400 FEG ESEM / EDAX Genesis X4M.

Using the SPI Module Sputter Coater equipment, samples were coated with an Au/Pd thin film by sputtering.

3. Results

3.1. Adsorption in continuous mode

3.1.1. Effect of pH

The breakthrough curves at pH 3.0 and 6.0 were compared for each inorganic antimony species. The pH values were selected because a previous study in batch mode indicated that pH 3 and 6 were the optimal values for Sb(V) and Sb(III) adsorption, respectively (Pintor et al., 2020a). The studies were conducted at an initial concentration of 1 mg L^{-1} and a temperature of 20 °C. The experimental results and Yan model predictions are shown in Fig. 1 and Table 1.

Adsorption of both antimony species was higher at pH 3, compared to the almost neutral solution at pH 6. For Sb(V), this pH effect follows batch equilibrium and kinetic studies shown in earlier research work, but for Sb(III), it was expected that adsorption would remain constant throughout a wide range of pH (Pintor et al., 2020a). Other results reported in the literature for iron-based adsorbents for Sb(V) indicated optimal pH values ranging from 3 to 5, with a significant decrease as pH increases above 5 (Deng et al., 2017). These results indicate that ICG may be a great candidate for treating acid effluents, such as acid mine drainage (Cappuyns et al., 2021; Guo et al., 2018; Manaka et al., 2007).

Furthermore, the effect of pH reduction from 6 to 3 was more evident for Sb(III) removal than for Sb(V) removal, as seen in Fig. 1. The maximum Sb(III) and Sb(V) adsorption capacities achieved were 13 ± 2 mg g^{-1} and 10 ± 1 mg g^{-1}, respectively, at pH 3. Meanwhile, the reduction in adsorption capacity from pH 3 to pH 6 was 89 % and 80 % for Sb(III) and Sb(V), respectively (Table 1). These findings are according to the literature that shows Sb adsorption to be speciation and pH-dependent (Bai et al., 2022; Dündar et al., 2022). However, it was not expected for this material, given the batch adsorption results referred earlier. Other studies have found a stronger Sb(V) than Sb(III) affinity toward green seaweed at pH 2 (Ungureanu et al., 2016). The optimal pH value for Sb(V) adsorption by Microcystis biomass was found to be 2.5–3.0 (Sun et al., 2014).

As the performance is reduced at higher pH levels, ICG is indicated for treating acid effluents such as acid mine drainage water containing high levels of antimony.

The ICG maximum removal capacity of Sb(III) in continuous mode was superior to that of quartz sand coated with Fe_3O_4 and graphene oxide (QFGO) of 2.88 – 6.09 mg g^{-1} as estimated by the Thomas model (Yang et al., 2015), brown seaweeds of 3.56 ± 0.06 mg g^{-1} as estimated

Table 1
Experimental and predicted breakthrough parameters on pH effect in Sb(III) and Sb(V) adsorption (C_i = 1 mg/L, T = 20 °C, FR = 5 mL min^{-1}; Bed height = 12 cm) (±standard error of the mean).

		Sb(III) pH 3	Sb(III) pH 6	Sb(V) pH 3	Sb(V) pH 6
Experimental	t_b (h)	126 ± 0.4	10.3 ± 0.2	98 ± 0.4	12.8 ± 0.3
	t_s (h)	295	65	263	50
	q_b (mg g^{-1})	7.9 ± 0.9	0.49 ± 0.03	6.2 ± 0.6	0.84 ± 0.06
	q_s (mg g^{-1})	13 ± 2	1.5 ± 0.2	10 ± 1	2.0 ± 0.2
	BV_b	639 ± 11	52 ± 1	501 ± 9	68 ± 2
	BV_s	1502 ± 87	331 ± 19	1339 ± 77	265 ± 15
	V_b (L)	37.7 ± 0.7	3.09 ± 0.08	29.5 ± 0.5	4.0 ± 0.1
	V_s (L)	88.5 ± 0.2	19.50 ± 0.06	78.9 ± 0.1	15.6 ± 0.1
	y_b (%)	99.973 ± 0.006	99.45 ± 0.08	99.2 ± 0.1	99.95 ± 0.01
	y_s (%)	71 ± 5	48 ± 4	63 ± 4	62 ± 4
	MTZ (cm)	6.9 ± 0.3	10.1 ± 0.5	7.5 ± 0.3	8.9 ± 0.4
	MTZ/Bed height	0.57 ± 0.03	0.84 ± 0.05	0.63 ± 0.04	0.74 ± 0.05
Yan Model	Q_{ya} (mg g^{-1})	13.0 ± 1.5	1.2 ± 0.1	9.9 ± 0.9	1.7 ± 0.1
	a_{ya}	6.1 ± 0.3	2.1 ± 0.1	4.3 ± 0.2	4.5 ± 0.3
	SE (mg g^{-1})	0.04	0.05	0.06	0.04
	R^2	0.984	0.953	0.972	0.990

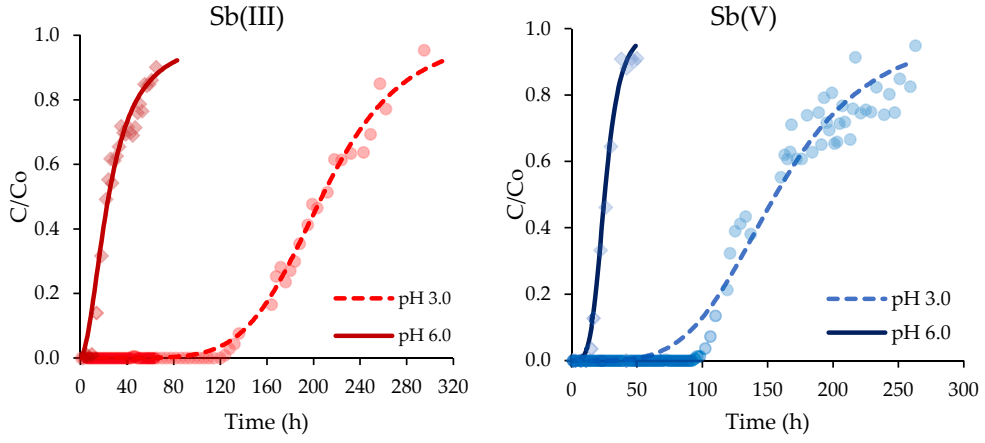

Fig. 1. pH effect on the Sb(III) and Sb(V) removal in the fixed-bed column (dots = experimental data, lines = Yan model predicted curves) (Inlet Sb(III)/Sb(V) concentration 1 mg/L; Bed height: 12 cm; Flow rate: 5 mL min^{-1}; Temperature: 20 °C).

by the Yan model (Ungureanu et al., 2017); but inferior to that of pine bark tannin resin of 31 ± 2 mg g^{-1} as estimated by the Yan model (Bacelo et al., 2022). Table 2 presents the maximum adsorption capacities reported in the literature.

3.2. Adsorption in batch mode

The pH effect on Sb(III) and Sb(V) adsorption onto ICG was previously investigated by this research group (Pintor et al., 2020a). In this study, the uptake of Sb(III) was stable in the range of 4–10, achieving a maximum adsorption capacity of 5.8 mg g^{-1} at pH 6.

Nonetheless, the investigation on the effect of pH in Sb(III) adsorption in continuous mode showed that the best adsorption capacity was found at pH 3 (Table 1). In order to confirm the best results of Sb(III) uptake onto ICG at pH 3, equilibrium and kinetics studies were conducted at this pH.

3.2.1. Equilibrium studies

The adsorption equilibrium of Sb(III) onto ICG was investigated at pH 3 and the results are shown in Table 3 and Fig. S3.

The Freundlich model presented a better fit to the experimental data like earlier equilibrium experiments conducted with Sb(III) onto iron-coated cork granulates (Pintor et al., 2020a). The Langmuir model showed a satisfactory fit and allowed us to estimate the maximum adsorption capacity as 8.2 ± 0.7 mg g^{-1}. This is over 40 % higher than the Langmuir estimate for Sb(III) removal reported for pH 6 as 5.8 ± 0.5 mg g^{-1} (Pintor et al., 2020a). Hence, the an increase in pH from 3 to 6 has a negative impact on the ICGs Sb(III) adsorption capacity.

Similar results were reported in studies showing that Sb(III) adsorption in zero-valent iron decreased from 15.3 mg g^{-1} to 10.9 mg g^{-1} as pH increased from 3 to 10 (Zhang et al., 2019) and from ~ 70 % to ~ 30 % as pH increased from 4 to 10 (Liu et al., 2020). However, the opposite behavior was also observed when an increase in pH caused an increase in adsorption capacity (Bacelo et al., 2022; Bacelo et al., 2018; Ungureanu et al., 2017; Zou et al., 2016). Also, no influence on Sb(III) removal was observed in the pH ranges from 2 to 12 (Verbinnen et al., 2013) or 3 to 9 (Yang et al., 2015) for other iron-based adsorbents.

The negative effect of pH increase on Sb(III) removal onto ICG can be caused by a higher concentration of H^+ in acidic solutions, which benefits the adsorption processes that may be taking part in the Sb(III) complexation with iron oxide surface groups (Guo et al., 2014; Pintor et al., 2020a). The uptake of Sb(III) is mostly pH-independent and occurs as neutral $Sb(OH)_3$. Electrostatic interactions do not play a significant role in the uptake of this species (Pintor et al., 2020a).

3.2.2. Kinetic studies

The kinetics models were fitted to the experimental results, however, only the pseudo-second-order model led to satisfactory results (Table S1 and Fig. S4). This indicates the occurrence of chemisorption, which is generally observed in iron-based adsorbents (Deng et al., 2017). A previous study (Pintor et al., 2020a) showed that the kinetics of Sb(III) adsorption at pH 6 (Ci = 10 mg/L) was very well described by the pseudo-second-order and Elovich models, with a kinetic constant k_2 value of 0.12 ± 0.03 g $mg^{-1}h^{-1}$. This value was lower than the k_2 found in this study of 0.51 ± 0.05 g $mg^{-1}h^{-1}$ (Ci = 15 mg/L), which indicates faster adsorption at pH 3.0 compared to pH 6.0.

Sb(III) adsorption kinetics initially presents a high adsorption rate for both initial concentration assays. For the lower concentration, Sb(III) equilibrium was achieved after 2 h. Still, in the first 15 min, the adsorption capacity of 0.53 ± 0.02 mg g^{-1} was very close (more than 90 %) to the equilibrium adsorption capacity of 0.580 ± 0.003 mg g^{-1} (Table S1). For higher concentrations, the kinetics was slower. The equilibrium was achieved after 48 h, leading to an adsorption capacity of 4.90 ± 0.07 mg g^{-1}, but after 4 h, the Sb(III) uptake was almost in equilibrium (90 %) with an adsorption capacity of 4.4 ± 0.9 mg g^{-1}. The initial concentration increase from 1 to 15 mg L^{-1} resulted in an approximately 8-fold increase in adsorption capacity at equilibrium. However, the adsorption capacity at equilibrium (8.2 ± 0.7 mg Sb(III) g^{-1}) according to Langmuir (section 3.2.1) was higher than that predicted by the pseudo-second-order model.

With other biosorbents, antimonite adsorption proceeded very rapidly. For example, in brown seaweeds, the equilibrium was also reached after 2 h but with good adsorption in the first 15 min ($0.022 \pm 0.002 < k_2 < 0.41 \pm 0.03$) (Ungureanu et al., 2017). By cyanobacterium *Synechocystis* sp., almost 50 % of the adsorption was achieved in 30 min, and equilibrium was reached after 1 h (k_2 = 0.052) (Biosorption of Antimony (Sb), 2011). In the first 20 min, antimonite was rapidly removed by iron-oxide-cottonwood biochar, and equilibrium was obtained after one hour (Zhang et al., 2022a).

Table 3
Equilibrium model parameters for Sb(III) at pH 3.0 (C_i = 10 mg/L) (±standard error of the mean).

		T = 20 °C
Langmuir	Q_{max} (mg g^{-1})	8.2 ± 0.7
	K_L (L mg^{-1})	3 ± 1
	R^2	0.937
	SE	0.7
Freundlich	K_F ($mg^{(1-1/n)}$ $L^{1/n}$ g^{-1})	5.3 ± 0.2
	n	3.2 ± 0.3
	R^2	0.982
	SE	0.4

3.3. Desorption in batch mode

In the study of desorption, only Sb(V) was examined, as it is the most prevalent oxidation state in the environment. Several eluents were

Table 2
Comparison of maximum adsorption capacities of antimony in fixed-bed columns.

	Species	pH	C_i (mg L^{-1})	Flow rate (mL min^{-1})	Bed height (cm)	Maximum adsorption capacity (mg g^{-1})	Ref.
Brown seaweeds	Sb(III)	7	25	4	17	3.56 ± 0.06	(Ungureanu et al., 2017)
Granular titanium dioxide (TiO_2)	Sb(V)	8.2	0.24	1.5	16	0.981	(Qiu et al., 2019)
Pine bark tannin resin	Sb(III)	6	9	3	10.5	31 ± 2	(Bacelo et al., 2022)
Quartz sand coated with Fe_3O_4 and graphene oxide (QFGO)	Sb(III)	7	40	8	10	6.03	(Yang et al., 2015)
Layered double hydroxide mineral, brucite (BRU)	Sb(III)	7.2	0.17	5.83	9.9	0.0004	(Runtti et al., 2023)
Nanoscale zero-valent iron (Fe0) supported on activated carbon (nZVI/AC)	Sb(V)	7	1	5	20	0.6275	(Zhu et al., 2021)
Fe-Mn binary oxides ($FMBO_3$)	Sb(V)	7	0.2	3.75	8.2	3.12	(Yang et al., 2019)
Bayoxide E33 (GFH)	Sb(III)	7	0.1	54.4	11.3	2.11	(Sazakli et al., 2014)
Iron-coated cork granulates (ICG)	Sb(III)	3	1	5	12	13.0 ± 1.5	This study
	Sb(V)	3	1	5	12	9.9 ± 0.9	

tested, at varying concentrations,in batch mode. The findings are summarized in Fig. 2 and Table S2. The acids outperformed the base and the salts, indicating Sb(V) desorption from ICG to be more favorable at very low pH levels. In Sb(V) desorption from cyanobacteria, acid eluents such as HCl 1 M (68.46 %) and citric acid 1 M (51.45 %) were found to be more efficient than NaOH 1 M (30.55 %) (Sun et al., 2014). Oppositely, the Sb(V) desorption from pine bark tannin resin was found to be higher using a basic solution of NaOH 0.1 M than using acid solutions of HCl (0.04 – 0.5 M) (Bacelo et al., 2022). Another study reported desorption rates of 65–75 % for ZVI decorated carbon nanotubes (CNT – Fe(0)) using HCl 0.05 M (Mishra et al., 2016).

The influence of eluent concentration on desorption was investigated for HCl, ascorbic acid, and citric acid. Each eluent behaved differently (Fig. S5). Between 0.1 to 1 M, the citric acid desorption efficiency remained nearly constant. Differently, the ascorbic acid efficiency rapidly increased from 0.001 to 0.05 M, reaching a maximum value of 66 ± 8 % at 0.1 M, and started to decrease from 0.1 M to 1 M. In the concentration range of 0.1 M to 1 M, HCl showed a different trend with a rise in efficiency until 81 ± 9 % but a propensity to reach a curve inflection at higher concentrations.

The Sb(V) desorption kinetics was studied using the eluents with the highest desorption efficiency at their most efficient concentration: ascorbic acid 0.1 M and HCl 1 M. The results from kinetic model fittings are shown in Table 4 and Fig. S6.

The pseudo-first-order model was the best fit for the experimental data for both desorbing agents, based on the observation of the correlation coefficient (R^2) and the standard error (SE), followed by the pseudo-second-order model and the Elovich model. The difference between each model fitting was higher when the inorganic acid was used.

Pseudo-first-order model estimations showed that both acids had comparable maximum desorption capacities (q_d) of 5.9 and 5.8 mg Sb (V) g^{-1} for HCl 1 M and ascorbic acid 0.1 M, respectively. However, the curve shapes differed, the curve of HCl 1 M being steeper than the curve of ascorbic acid. This difference in the curves' shapes is reflected in the contact time required to achieve roughly the maximum q_d, which was 16 h and 4 h for ascorbic acid 0.1 M and HCl 1 M, respectively. The kinetic constant k_1 of 0.86 ± 0.05 h^{-1} was also about four times higher for HCl 1 M than that for ascorbic acid 0.1 M of 0.22 ± 0.03 h^{-1}.

The maximum concentration of iron leached in the desorbed solution when using ascorbic acid 0.1 M and HCl 1 M was 23 ± 2 mg g^{-1} and 34 ± 2 mg g^{-1}, respectively, corresponding to approximately 70 and 100 % of the iron content in the adsorbent. As hydrochloric acid is more aggressive, the eluent chosen for desorption in continuous mode was the ascorbic acid 0.1 M. Although desorption using ascorbic acid 0.1 M can take longer it is a more environmentally friendly option, This makes it advantageous for desorption processes at a larger scale.

Table 4
Parameters obtained in the fitting of kinetic models to experimental data of desorption kinetics of Sb(V) from ICG.

Model	Parameters	*HCl*	Ascorbic acid
Pseudo-first-order	q_e (mg g^{-1})	5.7 ± 0.2	5.8 ± 0.3
	k_1 (h^{-1})	0.86 ± 0.05	0.22 ± 0.03
	R^2	0.994	0.976
	SE	0.2	0.4
Pseudo-second-order	q_e (mg g^{-1})	6.3 ± 0.3	7.0 ± 0.5
	k_2 (g $mg^{-1}h^{-1}$)	0.18 ± 0.04	0.03 ± 0.01
	R^2	0.963	0.973
	SE	0.4	0.4
Elovich	a (mg $g^{-1}h^{-1}$)	20 ± 14	2.4 ± 0.7
	b (g mg^{-1})	0.9 ± 0.2	0.57 ± 0.09
	R^2	0.852	0.963
	SE	0.8	0.4

The results revealed that the iron, together with the Sb(V), was desorbed from ICG, possibly posing a barrier to the application of the adsorbent in multiple adsorption cycles. The results differed from As(V) desorption from ICG, in which the basic eluents allowed for the highest desorption rates, and the iron coating was preserved sufficiently to withstand 3 and 5 adsorption/desorption cycles using NaOH 0.1 M and 0.01 M, respectively (Carneiro et al., 2022a).

The increased efficiency of HCl in removing Sb(V) can be attributed to Fe dissolution, and as a result, the removal of previously adsorbed Sb (V) complexed to iron. Runtti et al. (2022) suggest that the higher performance of HCl over NaOH to desorb Sb(V) from Mg-rich mineral adsorbents might be attributed to the forming of chloro-complexes. The affinity of Sb(V) to organic acids such as ascorbic acid, can be justified by the formation of neutral or cationic complexes, while the affinity of Sb(V) towards tartaric acid can be related to the formation of Sb(V)-tartrate complex (Thangaraj and Bhaskarapillai, 2020). The finding of this work is in line with the literature, in which citric acid was found to have lower effect on Sb release, compared to tartatric acid (Hu and He, 2017; Carneiro et. al., 2024).

The NaOH solutions that have proven to be effective eluents for As (V) from ICG were ineffective for desorbing Sb(V) from ICG. Variations

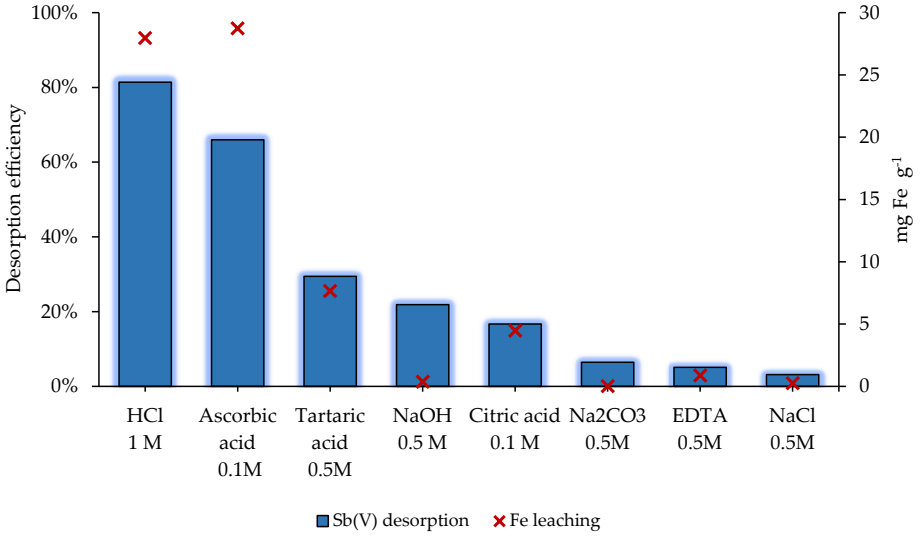

Fig. 2. Desorption efficiency of Sb(V) from ICG in batch mode and iron leaching for each eluent (S/L = 2.5 g/L; 20 °C; 10 ± 1 mg Sb(V)/g ICG; Initial iron loading = 29 ± 3 mg Fe/g ICG).

in the interaction between arsenate and OH^- and antimonate and OH^- in alkaline solutions can explain these differences. Antimony has a lower negative charge at high pH values (−1) compared to arsenic (−3) (Ungureanu et al., 2015). When the ICG surface charge becomes negative at alkaline pH values (its pHpzc is 6 (Pintor et al., 2018)), that can cause a more repulsive effect on arsenate, which might not be observed for antimonate. Another difference between antimony and arsenic that might be related to their different interaction with NaOH is the molecular structure. Sb(V) is arranged with oxygen in an octahedral geometry, while As(V) forms a lower spatial structure in a tetrahedral geometry (Simeonidis et al., 2017), leading to different adsorption (Pintor et al., 2020a) and, consequently, desorption mechanisms.

3.4. Desorption in continuous mode

We performed three adsorption–desorption cycles using 0.1 M ascorbic acid as a desorbing agent. Fresh ICG, regenerated ICG (after Sb desorption) and recycled ICG (after iron reloading) were used in the first, second and third adsorption cycles, respectively. The results are shown in Fig. 3 and Table S3.

The fresh ICG achieved a saturation adsorption capacity (q_s), according to the Yan model, of 7.5 ± 0.3 mg Sb(V) g^{-1}. Following adsorption, a desorption cycle was conducted for 7 h using ascorbic acid 0.1 M, resulting in a desorption capacity of 6.6 ± 0.2 mg Sb(V) g^{-1} (88 ± 4 %). Nevertheless, the iron leaching observed in batch desorption studies was also observed in continuous mode, with an iron removal of approximately 27.0 ± 0.8 mg Fe g^{-1}, 87 ± 4 % of the original iron content in the adsorbent. Following desorption, another AD cycle was carried out, and, as expected, the Sb(V) removal by the adsorbent was no longer feasible. This is a result of the absence of active sites from the iron coating leached in the previous desorption assay.

A new iron coating was carried out to regenerate and recycle the adsorbent. An AD cycle was run with recycled ICG, and a saturation adsorption capacity of 1.4 mg Sb(V) g^{-1} (Yan model) was achieved, about 80 % lower than the value obtained with fresh ICG. Another study using Fe(III) modified kapok fiber after adsorption/desorption cycles (using HCl as eluent), further reinvigorated with iron, showed a reduction in arsenic removal of 55 % compared to the one found using fresh adsorbent (Yeo et al., 2022). The authors suggested this might have been caused by damage in the structure of the natural adsorbent. For this reason, material characterization studies were carried out on ICG before and after adsorption and regeneration to understand possible modifications on the cork material that caused recycling to be ineffective.

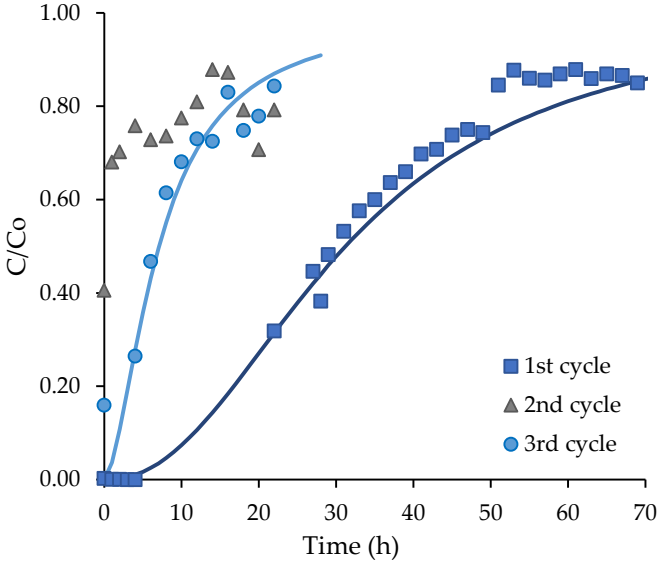

Fig. 3. Experimental and predicted (Yan model) breakthrough curves for Sb(V) adsorption from fresh ICG, regenerated ICG (after Sb desorption) and recycled ICG (after Fe reloading) (C_i = 5 mg/L; pH = 3.0, FR = 5 mL min^{-1}, 6 g of ICG, T = 20 °C).

3.6. Analysis of fresh, regenerated and recycled adsorbent

The iron content from fresh and recycled ICG was determined by acid digestion followed by FAAS. Results showed that recycled ICG had an iron loading of 13 ± 1 mg g^{-1}, which was 58 ± 4 % lower than the iron loading of fresh ICG (31 ± 1 mg g^{-1}). Therefore, the decrease in iron content in the adsorbent likely relates to the lower performance of the recycled adsorbents in terms of Sb(V) uptake.

SEM was used to compare the morphology and structure of the iron-coated cork granulates before and after desorption. Fig. 4 shows SEM micrographs of the ICG and recycled ICG after Sb(V) adsorption, and ICG after desorption using ascorbic acid 0.1 M and HCl 1 M. The Sb(V)-loaded ICG (Fig. 4ab) does not show a visual modification in comparison to fresh ICG (before adsorption) (Carneiro et al., 2022a; Pintor et al., 2018), with visible iron deposits and structured cell walls laid in "bricks". In contrast, recycled ICG has a different cell structure, with wrinkled cells and fewer iron deposits (Fig. 4cd). This structural alteration, accompanied by a reduction in iron content, explains the lower efficiency of the recycled material in adsorbing antimonate.

The iron layer is nearly eliminated in the samples after one adsorption–desorption cycle. However, it is still detectable in the ICG desorbed with ascorbic acid 0.1 M (Fig. 4e). Overall, it seems the wall composition was not altered after desorption, but the adsorbent structure became less compact, with the cells more open, which might be the reason influencing iron fixation. SEM micrographs of ICG samples after treatments with NaOH 0.1 M and NaOH 0.01 M revealed a stronger degradation in the adsorbent structure (Carneiro et al., 2022a). Nonetheless, the alkaline treatment did not remove as much iron from the cork cells as the acid eluents (Fig. 4ef).

The EDS results of ICG before and after desorption determined from the SEM images are shown (Fig. S7). Before desorption, the most abundant elements in ICG are Sb and Fe, with lower peaks of C and O. As predicted, Sb and Fe are much less present in the samples after desorption, with C and O remaining as the most abundant elements of the organic adsorbent.

4. Conclusions

This study evaluated the scaling up of antimony adsorption using iron-coated cork granulates (ICG), a carbon–neutral material for antimony removal. In continuous mode, the adsorption capacities were 13 ± 2 mg g^{-1} and 10 ± 1 mg g^{-1} for Sb(III) and Sb(V), respectively. However, pH sensitivity reduced performance at higher pH levels, suggesting ICG's preference for treating acid effluents such as acid mine drainage. Acids were effective for Sb desorption from ICG compared to NaOH, salts, or complexing agents. However, iron leaching during desorption impacted the reuse of ICG. Further research should be carried out using real water matrices to identify the interference of other contaminants in the antimony adsorption. For scaling-up the technology, improvements on the recovery/extraction techniques and environmental impact evaluations are necessary.

Funding

This work was supported by national funds through FCT/MCTES (PIDDAC): LSRE-LCM, UIDB/50020/2020 (https://doi.org/10.54499/UIDB/50020/2020) and UIDP/50020/2020 (https://doi.org/10.54499/UIDP/50020/2020); and ALiCE, LA/P/0045/2020 (https://doi.org/10.54499/LA/P/0045/2020). A. Pintor acknowledges her Junior Researcher contract CEECIND/01485/2017 (https://doi.org/10.54499/CEECIND/01485/2017/CP1399/CT0012) by FCT. M. Carneiro acknowledges her Ph.D. scholarship by FCT [2020.07233.BD]

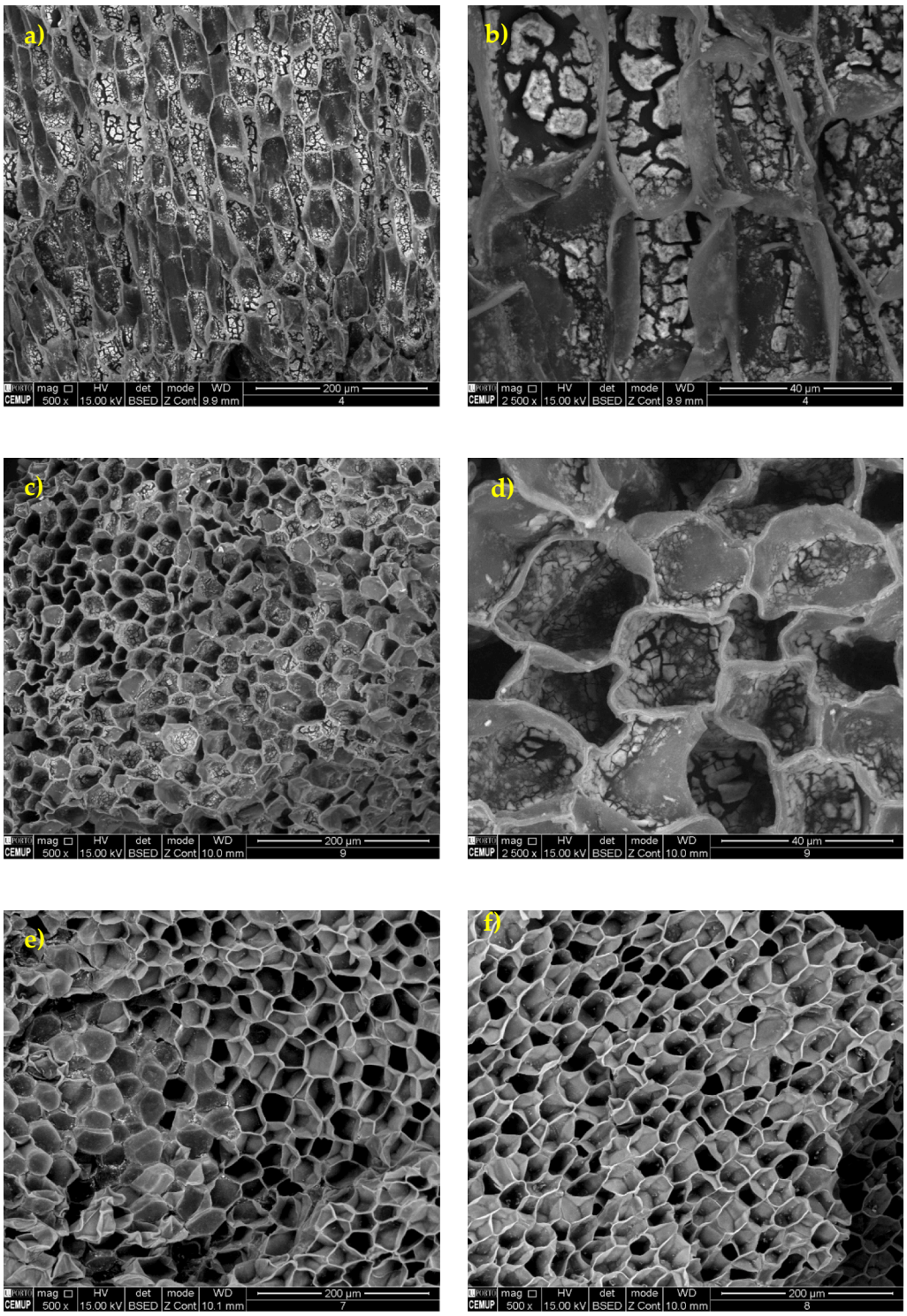

Fig. 4. SEM micrographs of: ICG after Sb(V) adsorption, a) 500x magnification, and b) 2500x magnification; recycled ICG after Sb(V) adsorption, c) 500x magnification, and d) 2500x magnification; ICG after Sb(V) desorption e) with acid ascorbic 0.1 M, 500x magnification and f) with HCl 1 M, 500x magnification.

(https://doi.org/10.54499/2020.07233.BD).

CRediT authorship contribution statement

Mariko A. Carneiro: Methodology, Validation, Formal analysis, Data curation, Investigation, Writing – original draft, Visualization. **Tânia A. Silva:** Investigation, Validation, Data curation, Visualization. **Pedro J.S. Teixeira:** Investigation, Validation, Data curation, Visualization. **Rui A.R. Boaventura:** Writing – review & editing, Funding acquisition. **Cidália M.S. Botelho:** Resources, Writing – review & editing, Funding acquisition. **Ariana M.A. Pintor:** Conceptualization, Methodology, Writing – review & editing, Supervision.

Declaration of competing interest

The authors declare that they have no known competing financial interests or personal relationships that could have appeared to influence the work reported in this paper.

Data availability

Data will be made available on request.

Acknowledgment

The authors acknowledge the Materials Center of the University of Porto (CEMUP) for the SEM/EDS analyses. The figures in this manuscript were created with BioRender.com.

Appendix A. Supplementary data

Supplementary data to this article can be found online at https://doi.org/10.1016/j.ces.2024.120207.

References

Adegoke, K.A., Akinnawo, S.O., Ajala, O.A., Adebusuyi, T.A., Maxakato, N.W., Bello, O. S., 2022. Progress and challenges in batch and optimization studies on the adsorptive removal of heavy metals using modified biomass-based adsorbents. Bioresource Technology Reports 19, 101115.

Bacelo, H., Vieira, B.R.C., Santos, S.C.R., Boaventura, R.A.R., Botelho, C.M.S., 2018. Recovery and valorization of tannins from a forest waste as an adsorbent for antimony uptake. J. Clean. Prod. 198, 1324–1335.

Bacelo, H., Santos, S.C.R., Ribeiro, A., Boaventura, R.A.R., Botelho, C.M.S., 2022. Antimony removal from water by pine bark tannin resin: Batch and fixed-bed adsorption. J. Environ. Manage. 302, 114100.

Bădescu, I.S., Bulgariu, D., Ahmad, I., Bulgariu, L., 2018. Valorisation possibilities of exhausted biosorbents loaded with metal ions – A review. J. Environ. Manage. 224, 288–297.

Bai, Y., Tang, X., Sun, L., Yin, W., Hu, G., Liu, M., Gong, Y., 2022. Application of iron-based materials for removal of antimony and arsenic from water: Sorption properties and mechanism insights. Chem. Eng. J. 431, 134143.

Biosorption of Antimony (Sb) by the Cyanobacterium *Synechocystis* sp. Polish Journal of Environmental Studies, 2011. 20(5): p. 1353-1358.

Biswas, B.K., Inoue, J.-I., Kawakita, H., Ohto, K., Inoue, K., 2009. Effective removal and recovery of antimony using metal-loaded saponified orange waste. J. Hazard. Mater. 172, 721–728.

Bortone, I., Santonastaso, G., Erto, A., Chianese, S., Di Nardo, A., Musmarra, D., 2021. An innovative in-situ DRAINage system for advanced groundwater reactive TREATment (in-DRAIN-TREAT). Chemosphere 270, 129412.

Canada, H., 1999. Guidelines for Canadian Drinking Water Quality: Guideline Technical Document – Antimony. Otawwa, Ontario.

Cappuyns, V., Van Campen, A., Helser, J., 2021. Antimony leaching from soils and mine waste from the Mau Due antimony mine. North-Vietnam. Journal of Geochemical Exploration 220, 106663.

Carneiro, M.A., et al., 2024. Arsenic and antimony desorption in water treatment processes: Scaling up challenges with emerging adsorbents. Science of The Total Environment 929, 172602. https://doi.org/10.1016/j.scitotenv.2024.172602.

Carneiro, M.A., Coelho, J.F.R., Pintor, A.M.A., Boaventura, R.A.R., Botelho, C.M.S., 2022a. Multi-cycle regeneration of arsenic-loaded iron-coated cork granulates for water treatment. J. Water Process Eng. 50, 103291.

Carneiro, M.A., Pintor, A.M.A., Boaventura, R.A.R., Botelho, C.M.S., 2022b. Efficient removal of arsenic from aqueous solution by continuous adsorption onto iron-coated cork granulates. J. Hazard. Mater. 128657.

Carvalho, P.C.S., Neiva, A.M.R., Silva, M.M.V.G., da Silva, E.A.F., 2014. Geochemical comparison of waters and stream sediments close to abandoned Sb-Au and As-Au mining areas, northern Portugal. Geochemistry 74, 267–283.

Chen, Z., Fu, D., Yuen Koh, K., Paul Chen, J., 2022. A new carbon nanotube modified by nano CaO2 for removal of chromate and phosphate from aqueous solutions. Chem. Eng. J. 446, 136845.

Cheng, M., Fang, Y., Li, H., Yang, Z., 2022. Review of recently used adsorbents for antimony removal from contaminated water. Environ. Sci. Pollut. Res. 29, 26021–26044.

Cidu, R., Biddau, R., Dore, E., Vacca, A., 2013. Antimony Dispersion at Abandoned Mines in Sardinia, Italy. Procedia Earth Planet. Sci. 7, 171–174.

Cole-Hamilton, D., 2020. The Role of Chemists and Chemical Engineers in a Sustainable World. Chemistry – A. European Journal 26, 1894–1899.

Dembele, S., Akcil, A., Panda, S., 2022. Technological trends, emerging applications and metallurgical strategies in antimony recovery from stibnite. Miner. Eng. 175, 107304.

Deng, R.-J., Jin, C.-S., Ren, B.-Z., Hou, B.-L., Hursthouse, A.S., 2017. The Potential for the Treatment of Antimony-Containing Wastewater by Iron-Based Adsorbents. Water 9, 794.

Dündar, O.A., Mehenktaş, C., Arar, Ö., 2022. Removal of Antimony(III) and Antimony(V) from water samples through water-soluble polymer-enhanced ultrafiltration. Environ. Res. 215, 114324.

Elovich, S.Y., Larionov, O.G., 1962. Theory of adsorption from nonelectrolyte solutions on solid adsorbents. Bulletin of the Academy of Sciences of the USSR, Division of Chemical Science 11, 198–203.

Epa, e.p.a.,, 2002. National primary drinking water regulations: long term 1 enhanced surface water treatment rule. Final Rule. Federal Register 67, 1811–1844.

European Union, C., 2020. Council Directive 2020/2184 of 16 December 2020. J. Eur. Commun. L, Off, p. 62.

Gan, Y., Ding, C., Xu, B., Liu, Z., Zhang, S., Cui, Y., Wu, B., Huang, W., Song, X., 2023. Antimony (Sb) pollution control by coagulation and membrane filtration in water/wastewater treatment: A comprehensive review. J. Hazard. Mater. 442, 130072.

Guo, W., Fu, Z., Wang, H., Song, F., Wu, F., Giesy, J.P., 2018. Environmental geochemical and spatial/temporal behavior of total and speciation of antimony in typical contaminated aquatic environment from Xikuangshan, China. Microchem. J. 137, 181–189.

Guo, X., Wu, Z., He, M., Meng, X., Jin, X., Qiu, N., Zhang, J., 2014. Adsorption of antimony onto iron oxyhydroxides: Adsorption behavior and surface structure. J. Hazard. Mater. 276, 339–345.

Herath, I., Vithanage, M., Bundschuh, J., 2017. Antimony as a global dilemma: Geochemistry, mobility, fate and transport. Environ. Pollut. 223, 545–559.

Hu, X., He, M., 2017. Organic ligand-induced dissolution kinetics of antimony trioxide. J. Environ. Sci. 56, 87–94.

Iqbal, M., Saeed, A., Edyvean, R.G.J., 2013. Bioremoval of antimony(III) from contaminated water using several plant wastes: Optimization of batch and dynamic flow conditions for sorption by green bean husk (Vigna radiata). Chem. Eng. J. 225, 192–201.

Jia, X., Zhou, J., Liu, J., Liu, P., Yu, L., Wen, B., Feng, Y., 2020. The antimony sorption and transport mechanisms in removal experiment by Mn-coated biochar. Sci. Total Environ. 724, 138158.

Kurt, M.A., Yıldırım, Ü., Güler, C., Güven, O., 2021. Antimony and arsenic contamination in water from antimonite mineralization: a case study from Turhal (Tokat, Northern Turkey). Environ. Forensic 1–13.

Lewińska, K., Karczewska, A., Siepak, M., Gałka, B., 2018. The Release of Antimony from Mine Dump Soils in the Presence and Absence of Forest Litter. Int. J. Environ. Res. Public Health 15, 2631.

Liu, S., Feng, H., Tang, L., Dong, H., Wang, J., Yu, J., Feng, C., Liu, Y., Luo, T., Ni, T., 2020. Removal of Sb(III) by sulfidated nanoscale zerovalent iron: The mechanism and impact of environmental conditions. Sci. Total Environ. 736, 139629.

Manaka, M., Yanase, N., Sato, T., Fukushi, K., 2007. Natural attenuation of antimony in mine drainage water. Geochem. J. 41, 17–27.

Mishra, S., Dwivedi, J., Kumar, A., Sankararamakrishnan, N., 2016. Removal of antimonite (Sb(iii)) and antimonate (Sb(v)) using zerovalent iron decorated functionalized carbon nanotubes. RSC Adv. 6, 95865–95878.

(MOH), M.o.H.o.t.P.s.R.o.C., 2006. Chinese National Standards GB 3838-2002: Sanitary Standards for Drinking Water Quality;, in: (SAC), S.A.o.C. (Ed.). China Water Risk:, Hongkong, China.

Nishad, P.A., Bhaskarapillai, A., 2021. Antimony, a pollutant of emerging concern: A review on industrial sources and remediation technologies. Chemosphere 277, 130252.

Nishad, P.A., Bhaskarapillai, A., Velmurugan, S., 2017. Towards finding an efficient sorbent for antimony: comparative investigations on antimony removal properties of potential antimony sorbents. Int. J. Environ. Sci. Technol. 14, 777–784.

Pintor, A.M.A., Vieira, B.R.C., Santos, S.C.R., Boaventura, R.A.R., Botelho, C.M.S., 2018. Arsenate and arsenite adsorption onto iron-coated cork granulates. Sci. Total Environ. 642, 1075–1089.

Pintor, A.M.A., Vieira, B.R.C., Boaventura, R.A.R., Botelho, C.M.S., 2020a. Removal of antimony from water by iron-coated cork granulates. Sep. Purif. Technol. 233, 116020.

Pintor, A.M.A., Vieira, B.R.C., Brandão, C.C., Boaventura, R.A.R., Botelho, C.M.S., 2020b. Complexation mechanisms in arsenic and phosphorus adsorption onto iron-coated cork granulates. J. Environ. Chem. Eng. 8, 104184.

Pintor, A.M.A., Brandão, C.C., Boaventura, R.A.R., Botelho, C.M.S., 2021. Multicomponent adsorption of pentavalent As, Sb and P onto iron-coated cork granulates. J. Hazard. Mater. 406, 124339.

Qi, P., Wang, Y., Zeng, J., Sui, K., Zhao, J., 2021. Progress in antimony capturing by superior materials: Mechanisms, properties and perspectives. Chem. Eng. J. 419, 130013.

Qiu, S., Yan, L., Jing, C., 2019. Simultaneous removal of arsenic and antimony from mining wastewater using granular TiO2: Batch and field column studies. J. Environ. Sci. 75, 269–276.

R, L., Rejiniemon, T.S., Sathya, R., Kuppusamy, P., Al-mekhlafi, F.A., Wadaan, M.A., Rajendran, P., 2022. Adsorption of heavy metals from the aqueous solution using activated biomass from Ulva flexuosa. Chemosphere 306, 135479.

Runtti, H., Luukkonen, T., Tuomikoski, S., Hu, T., Lassi, U., Kangas, T., 2022. Removal of antimony from model solutions, mine effluent, and textile industry wastewater with Mg-rich mineral adsorbents. Environ. Sci. Pollut. Res.

Runtti, H., Luukkonen, T., Tuomikoski, S., Hu, T., Lassi, U., Kangas, T., 2023. Removal of antimony from model solutions, mine effluent, and textile industry wastewater with Mg-rich mineral adsorbents. Environ. Sci. Pollut. Res. 30, 14139–14154.

Sazakli, E., Zouvelou, S.V., Kalavrouziotis, I., Leotsinidis, M., 2014. Arsenic and antimony removal from drinking water by adsorption on granular ferric oxide. Water Sci. Technol. 71, 622–629.

Serfor-Armah, Y., Nyarko, B.J.B., Dampare, S.B., Adomako, D., 2006. Levels of Arsenic and Antimony in Water and Sediment from Prestea, A Gold Mining Town in Ghana and its Environs. Water Air Soil Pollut. 175, 181.

Simeonidis, K., Papadopoulou, V., Tresintsi, S., Kokkinos, E., Katsoyiannis, I.A., Zouboulis, A.I., Mitrakas, M., 2017. Efficiency of Iron-Based Oxy-Hydroxides in Removing Antimony from Groundwater to Levels below the Drinking Water Regulation Limits. Sustainability 9, 238.

Sun, F., Yan, Y., Liao, H., Bai, Y., Xing, B., Wu, F., 2014. Biosorption of antimony(V) by freshwater cyanobacteria Microcystis from Lake Taihu, China: effects of pH and competitive ions. Environ. Sci. Pollut. Res. 21, 5836–5848.
Thangaraj, V., Bhaskarapillai, A., 2020. Organic acids modify the binding selectivity of crosslinked poly(ionic liquid) between Sb(III) and Sb(V). Mater. Today Commun. 25, 101507.
Thirunavukkarasu, A., Nithya, R., Sivashankar, R., 2021. Continuous fixed-bed biosorption process: A review. Chemical Engineering Journal Advances 8, 100188.
UN, 2016. Transforming our world: The 2030 agenda for sustainable development.
Ungureanu, G., Santos, S., Boaventura, R., Botelho, C., 2015. Arsenic and antimony in water and wastewater: Overview of removal techniques with special reference to latest advances in adsorption. J. Environ. Manage. 151, 326–342.
Ungureanu, G., Filote, C., Santos, S.C.R., Boaventura, R.A.R., Volf, I., Botelho, C.M.S., 2016. Antimony oxyanions uptake by green marine macroalgae. J. Environ. Chem. Eng. 4, 3441–3450.
Ungureanu, G., Santos, S.C.R., Volf, I., Boaventura, R.A.R., Botelho, C.M.S., 2017. Biosorption of antimony oxyanions by brown seaweeds: Batch and column studies. J. Environ. Chem. Eng. 5, 3463–3471.
Verbinnen, B., Block, C., Lievens, P., Van Brecht, A., Vandecasteele, C., 2013. Simultaneous removal of molybdenum, antimony and selenium oxyanions from wastewater by adsorption on supported magnetite. Waste Biomass Valoriz. 4, 635–645.
Wan, C., Wang, L., Lee, D.-J., Zhang, Q., Li, J., Liu, X., 2014. Fungi aerobic granules and use of Fe(III)-treated granules for biosorption of antimony(V). J. Taiwan Inst. Chem. Eng. 45, 2610–2614.
Who, 2022. Guidelines for drinking-water quality: incorporating the first and second addenda. World Health Organization, Geneva.
Yan, G., Viraraghavan, T., Chen, M., 2001. A New Model for Heavy Metal Removal in a Biosorption Column. Adsorpt. Sci. Technol. 19, 25–43.
Yang, K., Liu, Y., Li, Y., Cao, Z., Zhou, C., Wang, Z., Zhou, X., Baig, S.A., Xu, X., 2019. Applications and characteristics of Fe-Mn binary oxides for Sb(V) removal in textile wastewater: Selective adsorption and the fixed-bed column study. Chemosphere 232, 254–263.
Yang, X., Shi, Z., Liu, L., 2015. Adsorption of Sb(III) from aqueous solution by QFGO particles in batch and fixed-bed systems. Chem. Eng. J. 260, 444–453.
Yeo, K.F.H., Li, C., Dong, Y., Yang, Y., Wu, K., Zhang, H., Chen, Z., Gao, Y., Wang, W., 2022. Adsorption performance of Fe(III) modified kapok fiber for As(V) removal from water. Sep. Purif. Technol. 287, 120494.
Zhang, Y., Ding, C., Gong, D., Deng, Y., Huang, Y., Zheng, J., Xiong, S., Tang, R., Wang, Y., Su, L., 2021b. A review of the environmental chemical behavior, detection and treatment of antimony. Environ. Technol. Innov. 24, 102026.
Zhang, L., Dong, Y., Liu, J., Liu, C., Liu, W., Lin, H., 2022a. The effect of co-pyrolysis temperature for iron-biochar composites on their adsorption behavior of antimonite and antimonate in aqueous solution. Bioresour. Technol. 347, 126362.
Zhang, C., Jiang, H., Deng, Y., Wang, A., 2019. Adsorption performance of antimony by modified iron powder. RSC Adv. 9, 31645–31653.
Zhang, Y., O'Loughlin, E.J., Kwon, M.J., 2022b. Antimony Redox Processes in the Environment: A Critical Review of Associated Oxidants and Reductants. J. Hazard. Mater. 128607.
Zhang, X., Xie, N., Guo, Y., Niu, D., Sun, H.-B., Yang, Y., 2021a. Insights into adsorptive removal of antimony contaminants: Functional materials, evaluation and prospective. J. Hazard. Mater. 418, 126345.
Zhu, H., Huang, Q., Fu, S., Zhang, X., Yang, Z., Lu, J., Liu, B., Shi, M., Zhang, J., Wen, X., Li, J., 2021. Removal of Antimony(V) from Drinking Water Using nZVI/AC: Optimization of Batch and Fix Bed Conditions. Toxics 9, 266.
Zou, J.-P., Liu, H.-L., Luo, J., Xing, Q.-J., Du, H.-M., Jiang, X.-H., Luo, X.-B., Luo, S.-L., Suib, S.L., 2016. Three-Dimensional Reduced Graphene Oxide Coupled with Mn3O4 for Highly Efficient Removal of Sb(III) and Sb(V) from Water. ACS Appl. Mater. Interfaces 8, 18140–18149.